ACS NANO

www.acsnano.org

ARTICLE

Atomic-Level Structure Determines Electron–Phonon Scattering Rates in 2-D Polar Metal Heterostructures

Megan A. Steves, Siavash Rajabpour, Ke Wang, Chengye Dong, Wen He, Su Ying Quek, Joshua A. Robinson, and Kenneth L. Knappenberger, Jr.*

Cite This: *ACS Nano* 2021, 15, 17780–17789

Read Online

ACCESS | Metrics & More | Article Recommendations | Supporting Information

ABSTRACT: The electron dynamics of atomically thin 2-D polar metal heterostructures, which consisted of a few crystalline metal atomic layers intercalated between hexagonal silicon carbide and graphene grown from the silicon carbide, were studied using nearly degenerate transient absorption spectroscopy. Optical pumping created charge carriers in both the 2-D metals and graphene components. Wavelength-dependent probing suggests that graphene-to-metal carrier transfer occurred on a sub-picosecond time scale. Following rapid (<300 fs) carrier–carrier scattering, charge carriers monitored through the metal interband transition relaxed through several consecutive cooling mechanisms that included sub-picosecond carrier–phonon scattering and dissipation to the silicon carbide substrate over tens of picoseconds. By studying 2-D In, 2-D Ga, and a Ga/In alloy, we resolved accelerated electron–phonon scattering rates upon alloy formation as well as structural influences on the excitation of in-plane phonon shear modes. More rapid cooling in alloys is attributed to increased lattice disorder, which was observed through correlative polarization-resolved second harmonic generation and electron microscopy. This connection between the electronic relaxation rates, far-field optical responses, and metal lattice disorder is made possible by the intimate relation between nonlinear optical properties and atomic-level structure in these materials. These studies provided insights into electronic carrier dynamics in 2-D crystalline elemental metals, including resolving contributions from specific components of a 2-D metal-containing heterojunction. The correlative ultrafast spectroscopy and nonlinear microscopy results suggest that the energy dissipation rates can be tuned through atomic-level structures.

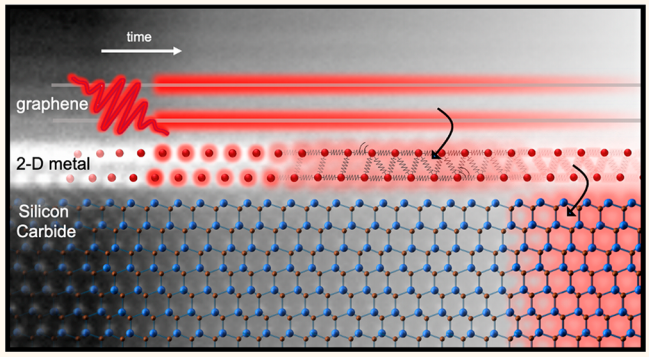

KEYWORDS: *2-D materials, electron dynamics, electron–phonon coupling, metals, nonlinear optical microscopy, correlative microscopy*

INTRODUCTION

Nanostructured metals offer a variety of potential applications in plasmonics,[1,2] nonlinear optics,[3−6] photodynamic therapy,[7] and photocatalysis,[8] among others. For many of these applications, overall performance is impacted by the efficiency with which nonequilibrium electrons are transduced by metals to disperse energy to the surroundings. A key intermediate step in the energy dissipation process is electron–phonon scattering, which occurs on the hundreds of femtoseconds to picosecond time scale for many metals.[9] The large majority of research on electron–phonon scattering in nanoscale metals has focused on coinage metals because of their superior environmental stability. For these systems, electron–phonon scattering rates reach bulk values as nanoparticle radii approach 10 nm, leaving limited options for tuning electron–phonon coupling strengths.[10] However, upon sub-nanometer 3-D spatial confinement, metal nanoclusters exhibit complex dynamics that include wavelength-dependent electron–phonon coupling strengths.[4,11,12] Therefore, the exploration of metals in the sub-to-few nanometer range may impact energy management materials.

Recently, heterostructures incorporating two-dimensional films of indium and gallium have been reported to be air-stable

Received: July 13, 2021
Accepted: October 14, 2021
Published: October 19, 2021

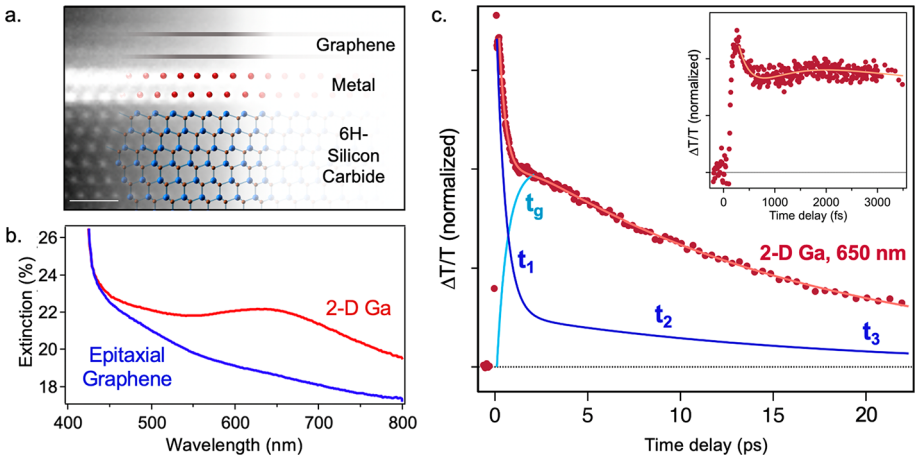

Figure 1. Structure, optical properties, and dynamics of 2-D Ga. (a) Cross-sectional scanning transmission electron microscopy (STEM) image of 2-D PMet and schematic indicating three components of the heterostructure. (b) Linear extinction spectrum of 2-D Ga PMet (red) and epitaxial graphene on SiC (blue). The epitaxial graphene spectrum was offset vertically to account for different SiC thicknesses in the two samples and aid in comparison. (c) Transient transmission results for 2-D Ga at a pump/probe wavelength of 650 nm. Fit components corresponding to the results reported in Table 1 are overlaid and normalized to the experimental data as a guide to the eye. Inset shows transient transmission data at 650 nm for another 2-D Ga sample to aid the viewer in visualizing the ~ picosecond signal growth (t_g).

for months.[13] These structures, synthesized through confinement heteroepitaxy (CHet), consist of a few crystalline atomic layers of a group III metal, which form epitaxial to a 6*H*-silicon carbide substrate and are capped by bilayer graphene (Figure 1a). This advancement greatly extends the range of nanoscale metals that can be studied outside of a vacuum. Our previous research showed that these metals adopt lattice structures atypical of bulk and are characterized by large lattice strain; an approximate 10% change in lattice parameters occurs over three atomic layers. This large strain is a consequence of metal growth between the silicon carbide and graphene layers, which promotes covalent bonding at the high-energy SiC interface and templates the metal into a highly strained hexagonal lattice in contrast with the orthorhombic or tetragonal lattices of bulk Ga and In, respectively. Metal−metal bonding occurs in the polar metal layer, and van der Waals interactions dominate at the graphene interface.[13,14] These polar metal heterostructures (PMets) are noted for their optical and physical properties including superconductivity, large nonlinear optical yields, and potential ε-near-zero responses.[13−15] The large strain that underlies their polar nature may also lead to efficient energy dissipation rates. Because these metals are confined to a two-dimensional platform, they may have other technological benefits with regard to scalability and incorporation into multicomponent materials. Building on the success of van der Waals two-dimensional semiconductor heterojunctions,[16−18] 2-D metals that can be easily incorporated into heterostructures with tunable electronic and optical properties could overcome many of the scalability challenges presented by 3-D colloids and may provide a thin layer for improved thermal energy management. In particular, interlayer carrier transfer in these heterostructures could improve graphene-based technologies by transiently modulating sheet carrier densities and reducing thermal fouling *via* rapid metal-mediated cooling. Two-dimensional metals may also exhibit advantages such as plasmon modulation, superconductivity, and ε-near-zero properties over other 3-D metal nanostructures.[13,19−21]

Here, we describe the electronic carrier dynamics of 2-D PMets. While the ultrafast dynamics of colloidal 3-D and bulk metals are well-studied,[9,22−24] the influences of 2-D metal confinement on carrier dynamics have not been reported. Through nearly degenerate ultrafast spectroscopy that excited and monitored metal interband transitions, carrier dynamics due to 2-D metal excitation were resolved and distinguished from carrier transfer from the graphene capping layer to the 2-D metal. Measurements on 2-D Ga, In, and GaIn alloys demonstrate that the choice of metal and composition influences energy dissipation in the 2-D polar metal heterostructure (PMet). The connection between the nonlinear optical response and the lattice symmetry was leveraged to elucidate the effects of alloying on the structure of the 2-D PMet through polarization-resolved second harmonic generation (SHG) microscopy. The changes to 2-D metal structure upon alloying are connected to faster electron cooling. Combined, these results point to the ability to manipulate energy dissipation in 2-D polar metal heterostructures and potentially control interfacial energy transfer in more complex heterostructures.

RESULTS AND DISCUSSION

The absorption spectrum of the 2-D Ga heterostructure features a broad peak in the visible region, centered at approximately 640 nm (Figure 1b). This peak is not observed in the absorption spectrum of epitaxial graphene (EG) on SiC and so is attributed to the metal component of the heterostructure. The energy of this peak agrees well with previous determinations of the dielectric functions of 2-D Ga obtained from ellipsometry, which attribute this feature to an interband transition of the metal.[15] This interband transition is sensitive to the choice of metal intercalant, typically exhibiting a 50 nm red shift for indium with respect to gallium (Figure S1). The 2-D alloy interband transition energy can be tuned by the metal composition,[25] and the absorption peak is located between the 2-D In and 2-D Ga peaks (Figure S1).

The electronic relaxation dynamics of 2-D PMets were investigated using femtosecond time-resolved transient absorption spectroscopy with nearly degenerate pump and probe wavelengths in the visible and near-infrared. Pump and probe beams were overlapped at the sample, and the differential transmission signal was collected as a function of the pump−

https://doi.org/10.1021/acsnano.1c05944
ACS Nano 2021, 15, 17780−17789

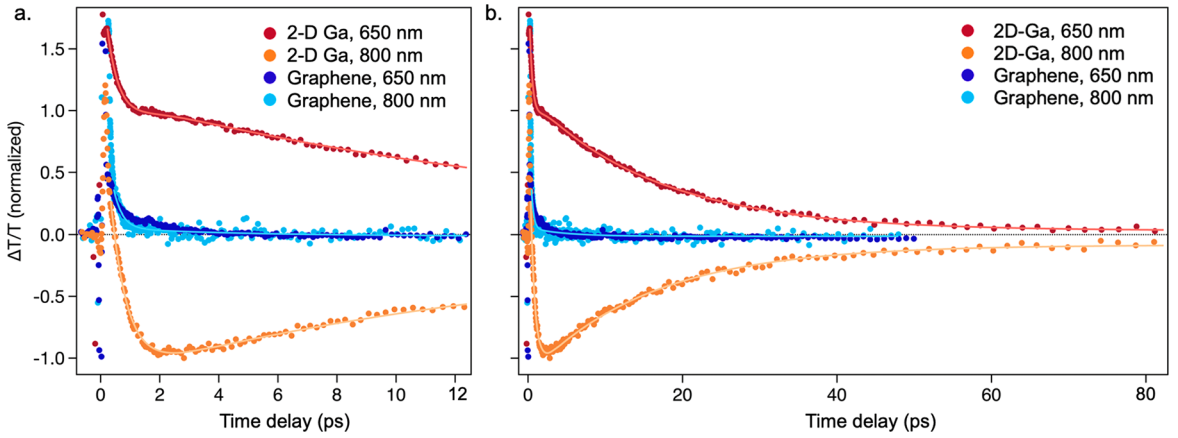

Figure 2. Wavelength-dependent dynamics of 2-D Ga and epitaxial graphene. Transient transmission traces for pump/probe wavelengths of 650 and 800 nm for 2-D Ga (red and orange, respectively) and epitaxial graphene (dark blue and light blue, respectively) on SiC at relatively (a) short and (b) long times after excitation.

Table 1. Summary of Fitting Time Constants

	polarity	indium	Ga/In (48% In)	gallium
t_1	positive	650 ± 100 fs	130 ± 24 fs	430 ± 130 fs
t_2	positive	39 ± 5 ps	14.2 ± 2.4 ps	16.5 ± 3.4 ps
t_3	positive	>150 ps	>150 ps	>150 ps
t_g	negative	680 ± 110 fs	1500 ± 400 fs	470 ± 170 fs
frequency			34 ± 5 cm^{-1}	

probe time delay. Further details are given in the Experimental Section. Although the pulses used in these measurements are <100 fs, strong interference signals from the pump/probe pulses around zero delay time likely obscure the rapid electron−electron scattering process, which we estimate to be complete within 300 fs. Therefore, we treated 300 fs as the effective instrument response time and limited our analysis to signals at delay times >300 fs.

The transient absorption results from 2-D Ga are first described as a general case (Figure 1c). The transient absorption signal from 2-D Ga using 650 nm pump/probe wavelengths for interband-resonant excitation/detection is dominated by a positive-amplitude bleach signal, which evolves over four characteristic time scales. The time-dependent transient signal amplitudes are overlaid with fitting results that reflect the four carrier relaxation steps in Figure 1c. After the initial excitation and instrument response time, the intense transient bleaching rapidly recovers (blue line, t_1 in Figure 1c). By approximately 2 ps pump−probe time delay, another simultaneous, kinetic process overtakes the bleach recovery and causes the bleach amplitude to intensify (becoming more positive). This picosecond growth of the bleach component is shown by the light blue line, t_g, in Figure 1c. The growth also causes an inflection of the differential transmission amplitude in the pump−probe trace monitored at 650 nm, which is visible in Figure 1c (inset) and Figure 2a (red trace). These two simultaneous subpicosecond and picosecond processes are followed by a slower bleach recovery persisting over tens of picoseconds (t_2, Figure 1c), which eventually plateaus into a third (t_3, Figure 1c), slower decay that persisted for the 150 ps pump−probe range of the experiments. Table 1 summarizes the time constants obtained from fitting to a four-component kinetic model (Experimental Section). Measurements were also carried out using 800 nm pump and probe wavelengths (Figure 2). Similar to interband excitation, 800 nm pumping induces a transient bleach that recovers on a subpicosecond time scale. In general, the 650 and 800 nm excitations result in qualitatively similar relaxation processes. At both wavelengths, the transient signal grows on a picosecond-time scale and subsequently decays with two time constants of tens of picoseconds and over 150 ps. One notable difference, however, was that, following the rapid 800 nm induced transient bleaching, an inversion in signal polarity was observed (Figure 2). The similar dynamics but opposite polarity make the transient absorption data at 650 and 800 nm appear as mirror images in the plot in Figure 2 (orange and red traces).

Having described the general electronic cooling rates, contributions from each of the 2-D PMet components (*i.e.*, SiC, 2-D metal, and bilayer graphene) to the transient signals are considered. Because the bandgap of 6*H*-SiC at 3.0 eV is above the pump and probe energies used in these measurements, it is assumed that the SiC substrate does not contribute to the transient absorption signal measured here. The differential signal from a SiC blank (Figure S2) is short-lived and likely arises from interference between the pump and probe pulses within the SiC dielectric around time zero. At delay times >400 fs, there is no signal from the SiC blank, indicating there is no contribution from multiphoton absorption in SiC to the transient signals we observe in the 2-D PMet heterostructure.

Having ruled out contributions from the SiC substrate, contributions from the few atomic layers of Ga and bilayer graphene to the differential transmission are considered. The peak in the 2-D Ga extinction spectrum at 640 nm is estimated to have an extinction of about 2%, which is similar in magnitude to the approximately 4% absorption of bilayer graphene at visible wavelengths.[26] Because both the 2-D metal layer and graphene absorb in the visible region, we cannot attribute the differential transmission signal to either component on the basis of the linear extinction spectrum

https://doi.org/10.1021/acsnano.1c05944
ACS Nano 2021, 15, 17780−17789

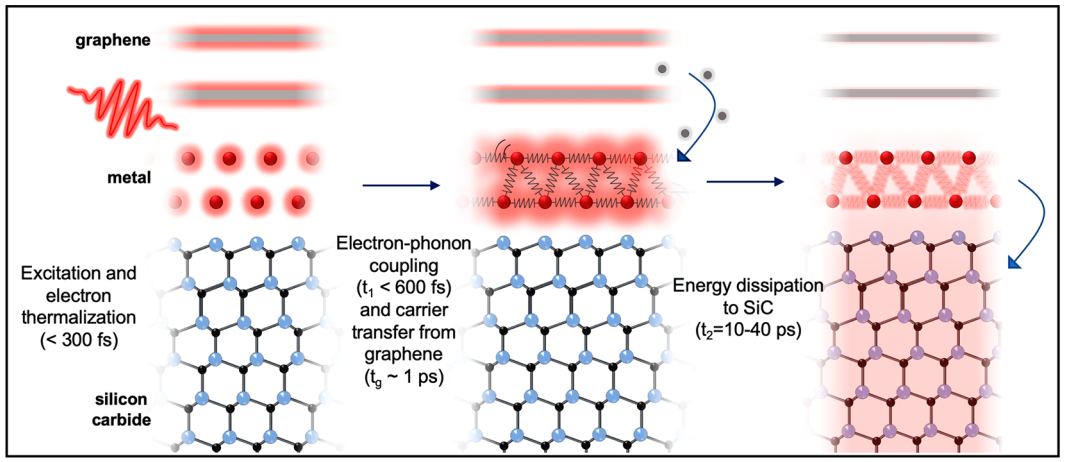

Figure 3. Carrier dynamics in 2-D PMets. After photoexcitation, carriers in both the 2-D metal and graphene are excited, and electrons thermalize rapidly. Within the metal, electron−phonon coupling occurs in under 600 fs and carriers excited in graphene transfer to the metal layers. Finally the metal dissipates energy into the SiC substrate (10−40 ps).

alone and must assume that both components are impulsively excited by the short laser pulses. However, the wavelength-dependent transient absorption signals provide insight into the contributions of each component. Figure 2 shows the transient signal for the 2-D Ga heterostructure and an EG/SiC standard for nearly degenerate pump/probe pulses centered at 650 and 800 nm. For EG/SiC, there is an initial bleach of the graphene absorption caused by Pauli blocking of interband transitions, which decays and converts to a negative ΔT as the electrons cool and a low-amplitude differential absorption of intraband transitions dominates (Figure S3).[27] As expected, the transient response of EG/SiC at both 650 and 800 nm pump/probe wavelengths is similar.

The wavelength-independent transient response of EG/SiC contrasts with the wavelength-dependent signals measured for the 2-D Ga PMet (Figure 2). Therefore, we conclude that the differences observed for the PMet at 650 and 800 nm excitation/detection primarily reflect electronic cooling of the 2-D metal component of the heterostructure. The initial bleach observed for 2-D PMets is attributed to Pauli blocking of the metal interband transition; although detuned, the 800 nm light still has nonzero spectral overlap with the broad PMet interband transition. The mirrored dynamics in the 650 and 800 nm transient absorption data in Figure 2 (red and orange traces) is a common feature of transient spectroscopy measurements of nanoscale metals, where a positive signal arises from absorption by excited charge carriers.[28,29] This observation supports the attribution of the transient signal to Pauli blocking and excited state absorption of metal carriers. Due to the spectral overlap between the graphene and metal components in the visible region, we cannot completely disentangle the 2-D metal and graphene contributions to the signal. However, because of the signal inversion when probing at 800 nm compared to 650 nm, which is not expected for graphene, we assume that the transient absorption signal primarily probes the metal component of the heterostructure.

On the basis of the polarities and time constants of the transient signals, we assign the first decay component (t_1) to subpicosecond electron−phonon coupling within the metal of carriers excited by the PMet interband transition. The second decay component (t_2) is assigned to energy dissipation from the metal to the SiC substrate. This decay component is fit to a time constant of approximately 15 ps. A similar decay component was observed for gallium nanoparticles in SiO_x.[30] The presence of a nonmonoexponential decay for the long time dynamics (modeled here as a biexponential decay with 15 and >150 ps time constants) likely indicates cooling processes determined by contributions from both interfacial thermal conductivity and heat diffusion in the substrate.[31] The approximately 1 ps growth component (t_g) is assigned to a transfer of carriers initially excited in graphene to the 2-D metal and, as such, is treated separately from the three electronic cooling steps resulting from metal interband excitation. It is possible that the growth is due to another metal relaxation step, *e.g.*, electron−electron scattering. However, given the time scale of the growth step, which is slower than electron−phonon scattering, it is more likely that the growth results from carrier transfer through the following mechanism. Although the bleach at ~650 nm primarily probes the 2-D metal through the visible interband absorption feature, the capping graphene layers are also excited by the pump pulse even though their differential response is relatively low. Photoexcited carriers in graphene can then transfer to the 2-D metal layers, resulting in additional Pauli blocking of the interband transition and a corresponding increase in the bleach signal. The picosecond time scale for this process is consistent with the optical phonon lifetime in graphene. All of the carrier relaxation processes are illustrated in Figure 3.

Next, the dynamics of the 2-D Ga heterostructure are compared to prior measurements on gallium nanoparticles. Previous results from solid and liquid Ga nanoparticles smaller than 20 nm in diameter indicated that electronic relaxation in these systems follows the steps typically observed in noble metal nanoparticles: after an initial instrument-response-limited rise in transient signal as excited electrons equilibrate to form a hot electron gas, subsequent picosecond cooling occurs *via* electron−phonon coupling.[30,32] The electron−phonon coupling time is described by a two-temperature model (TTM).[33] In small Ga nanoparticles, the characteristic electron−phonon coupling time is dependent on the size of the nanoparticle, with the rate increasing as particles become smaller.[32] The time constants observed for the nanoparticles are comparable to the initial fast decay observed in 2-D metals (t_1). The subpicosecond time scale is also similar to electron−phonon coupling times observed in other 2-D systems, such as graphene.[34]

https://doi.org/10.1021/acsnano.1c05944
ACS Nano 2021, 15, 17780−17789

Although the time scales for electron−phonon coupling of the 2-D PMets are in agreement with those of 3-D metal nanoparticles, differences in the excitation power dependence were observed (Figure S4). Typically, electron−phonon coupling times in metals are expected to have a linear dependence on the pump fluence, following from the TTM and the linear dependence of the electron heat capacity, C_e, on the electron temperature, T_e, described by $C_e(T_e) = \gamma T_e$. The Figure S4 data show the power dependence observed for a graphene-capped 2.5 nm-thick gold film on a SiC substrate compared to the 2-D PMets. The Figure S4 data were obtained using the same laser system. In the case of the gold film, a linear pulse energy dependence of the electron−phonon scattering rates was evident. In contrast, the 2-D PMets exhibit no resolvable dependence of the electron−phonon scattering rate (t_1) on laser power. Deviations from the TTM may occur for two primary reasons: (1) the density of photogenerated charge carriers may exceed the available phonon bath and (2) the electron heat capacity of the materials may not scale linearly with electronic temperature in the range studied. In order to assess these two cases, we estimated the pump fluence on the basis of the focusing optics used in the experiments, which result in pump beam waists of several hundred microns. Here, a typical pulse energy of ≥2 nJ/pulse was required to obtain sufficient signal to accurately quantify t_1. Therefore, all pump fluences reported here are estimated to be over 0.1 μJ/cm^2. In case 1, which corresponds to saturation of the phonon bath, a "hot phonon effect" is expected, and the measured electron−phonon coupling time constant will be limited by the phonon lifetime. The hot phonon effect has been observed in 2-D materials such as graphene with visible pump fluences in the mJ/cm^2 range.[34] While the pump fluences in this work do not approach the mJ/cm^2 regime, the increased carrier density of 2-D metals (~10^{14}/cm^2) compared to graphene (~10^{12}/cm^2)[13] can be expected to result in more excited carriers in the 2-D metal heterostructures for a given pump fluence. Therefore, the increased carrier density, along with differences in the phonon modes of the 2-D PMet may alter the saturation fluence at which the hot phonon effect becomes relevant in our experiments. In case 2, the temperature at which the linear approximation is no longer valid varies depending on the electronic density of states near the Fermi level but can be under 100 K in metals such as Ni.[35] Therefore, the nonlinearity of the electron heat capacity may contribute to the lack of a linear fluence dependence for the electron−phonon coupling time, t_1. On the basis of the lack of a power dependence in the 2-D PMet time constants, we conclude that our experiments are in a regime where the hot phonon effect, nonlinear electron heat capacity, or both contribute to the dynamics of the system. The observation of this difference in the electronic properties of these elemental 2-D metals when compared to 3-D metals such as gold and gallium represents an interesting distinction between these systems.

Next, the influence of metal intercalant and composition on the electronic relaxation dynamics of the PMets is described. In addition to 2-D Ga, transient absorption spectroscopy was performed on 2-D In and a 50% 2-D Ga/In alloy. Similar absorption features are observed in the spectra of 2-D In and the 2-D alloy (Figure S1). Transient absorption data for all samples show similar features to the 2-D Ga sample already discussed (Figure 4). Comparing the fitting results obtained for different metal compositions (Table 1), it is apparent that

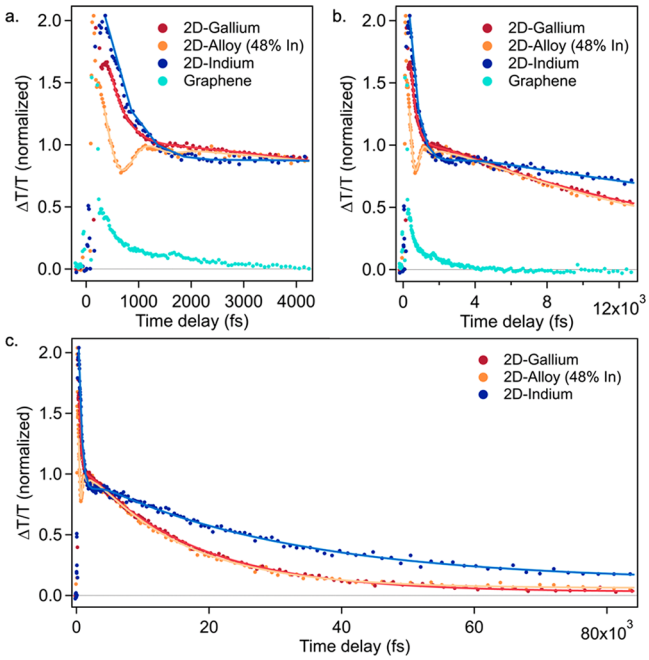

Figure 4. Dynamics of 2-D PMets at 650 nm. Comparison of the transient transmission results for 2-D Ga (red), 2-D In (dark blue), and a 2-D alloy with 48% In and 52% Ga (orange) at relatively (a) short, (b) medium, and (c) long times after excitation.

t_1 is shorter for the 2-D metal alloy compared to monometal systems. Additionally, a longer time constant for carrier transfer from graphene (t_2) is obtained for the alloy. Heat dissipation (t_2) occurs more slowly for 2-D In than for 2-D Ga, suggesting a smaller interfacial conductivity in the 2-D In heterostructure. At long time delays, the alloy behaves similarly to the 2-D Ga, suggesting that heat dissipation in alloys occurs through the more efficient Ga channel. This result is consistent with research on metal particles of gallium, indium, and their alloys, which indicates that the thermal conductivities of indium−gallium alloys are more similar to monoelemental gallium than for monoelemental indium.[36] However, the faster heat dissipation in 2-D Ga contrasts with expectations for bulk group III metals, where Ga has a lower interfacial conductivity than In.[36] This mismatch between bulk-based expectations and the data on few-atomic-layer films is unsurprising given the differences in crystal structure between bulk and 2-D indium and gallium.[13] The atomic size may play a role in the different interfacial conductivities of 2-D In and Ga; the acoustic impedance of 2-D In and Ga may also contribute to the interfacial conductivity, as it does in noble metal nanoparticles.[31] Further theoretical predictions of the acoustic properties of 2-D metals may clarify the contributions to the heat dissipation dynamics of 2-D Ga and In.

We attribute the increased electron−phonon scattering rates in 2-D alloy heterostructures to increased structural disorder. An acceleration of electron−phonon scattering with increasing density of defects occurs in graphene, noble metal nanoparticles, and thin films.[37−40] The importance of the metal phonon modes in determining the early time dynamics is also suggested by the presence of oscillatory features observed in the transient absorption data. In 2-D alloys, a prominent oscillation is observed in the time-domain data. Fitting of these oscillations by incorporating a damped sine function with the previously discussed exponential decay reveals a frequency of

https://doi.org/10.1021/acsnano.1c05944
ACS Nano 2021, 15, 17780−17789

approximately 35 cm^{-1}. Oscillations are observed in the time-domain data from some 2-D Ga samples but with lower relative amplitudes than in 2-D alloys (Figure 5 and Figure S5). The oscillations measured for 2-D Ga exhibited a slightly lower frequency (28 cm^{-1}) than the 2-D alloys. Low-frequency oscillations in transient absorption data can arise from stimulated Raman scattering or from displacive excitation of coherent phonons.[41] Using a first-principles Green's function approach, we can attribute both of the observed low-frequency oscillations to in-plane shear modes, as shown in the insets in Figure 5. Our calculations show that, in these systems, most of the low-frequency phonon modes with nonzero frequencies are in-plane shear modes. The experimentally determined frequency oscillations are close to those for in-plane shear modes with phonon wavevectors corresponding to ~1 nm domain sizes (Figure S6), suggesting the important role of disorder in the phonon dynamics of these systems.

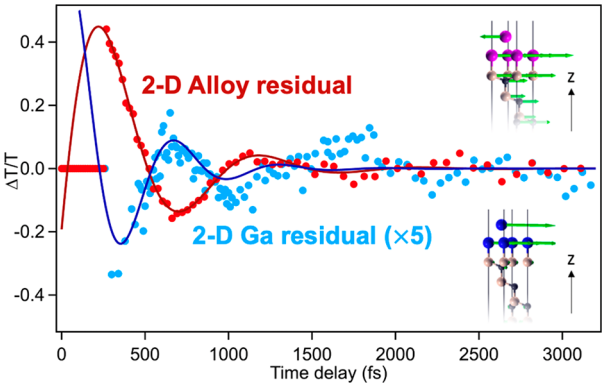

Figure 5. Coherent dynamics in 2-D PMets. Residuals from fitting transient transmission data reveal oscillations that are fit with a damped sin function. The 2-D Ga residual is multiplied by a factor of 5 to aid comparison. The frequencies of the oscillations for both the 2-D Ga and the 2-D alloy samples correspond to low-frequency shear modes in our calculations. The phonon displacements of these shear modes are shown as insets in the respective panels, where the z direction denotes the out-of-plane direction. Blue, purple, pink, and black balls represent Ga atoms, alloy atoms, silicon atoms, and carbon atoms, respectively.

The Figure 5 data also show a phase shift for the coherent phonon dynamics when 2-D Ga is compared to 2-D Ga/In alloys. This observation suggests that, although both monometal and alloy systems couple to the same phonon shear mode, the excitation mechanisms may differ. Typically, a displacive mechanism excites high-symmetry phonon modes, and asymmetric modes can be excited directly through stimulated Raman. The mechanisms can be distinguished by their phase with respect to the maximum of the exciting laser pulse. While displacive oscillations should have a temporal dependence of $\cos(\omega t)$, stimulated modes will have a dependence of $\cos(\omega t + \pi/2)$. The complex instrument response in the transient absorption data leads to some ambiguity in determining the absolute phase of these oscillations with respect to the pump pulse. However, fitting with a damped sine function reveals a relative phase difference of 0.36π between the oscillations in the residuals of 2-D Ga and the 2-D alloy, suggesting that displacive modes dominate the transient signal in one case and stimulated Raman processes dominate in the other. The phase difference between the 2-D Ga and 2-D alloy PMets can be seen in the overlay given in Figure 5. While these oscillations are present only occasionally and with low amplitudes in 2-D Ga and In, they are prominently observed in the transient absorption data for all 2-D alloys studied. Taken together, the accelerated electron–phonon scattering rates and intensified coherent phonon oscillations suggest strong electron–phonon interactions for the alloy structures. A possible explanation for the stronger electron–phonon coupling is through symmetry breaking from an added disorder in the 2-D alloys. This reduced symmetry may allow for more efficient excitation of phonon shear modes. Further study is required to elucidate precisely how material structure influences the phonon excitation mechanism.

Polarization-resolved SHG microscopy confirmed that increased structural disorder in 2-D alloys resulted in faster electron–phonon coupling and more intense coherent phonon oscillations. Our previous work demonstrates the close relationship between the atomic-level structure and polarization-dependent SHG of 2-D polar metal heterostructures.[14] Polarization-dependent SHG microscopy was performed by collecting the SHG-detected image while varying the excitation and emission polarization planes (α and β, respectively), which were referenced to the i-axis of the lab frame. The excitation and emission polarization planes were adjusted with a waveplate and polarizer, respectively (Figure 6g). 2-D In and Ga display spatially alternating regions of signal with distinct polarization dependences. These regions are the result of in-plane symmetry breaking at step edges combined with a lattice orientation that persists over an entire terrace, typically persisting for microns. The lattice orientation is determined by the interaction of the metal atoms with the SiC substrate. Rotation of the lattice at each step edge results in distinct deviations from the expected C_{3v} point group symmetry, allowing us to distinguish the changing metal orientation using polarization-dependent far-field SHG microscopy. In 2-D Ga/In alloys, however, these distinct polar patterns were not observed. While the SHG-detected images from 2-D In, Ga, and alloys show similar features, with micron scale terraces separated by dark step edges, the terraces of the alloy samples all demonstrate the nearly isotropic excitation polarization dependences expected for a crystal with C_{3v} symmetry (Figure 6).

The lack of an observable defect in the SHG polar patterns for 2-D Ga/In is attributed to increased structural disorder in the 2-D metal upon alloying. Spatially alternating polarization patterns are observed in monoelemental 2-D In and Ga due to templating by the SiC substrate, which causes the persistence of the metal lattice rotation across an entire micrometer-wide terrace.[14] Because of this strong metal–substrate interaction, the metal layers in 2-D In and Ga retain the same lattice rotation over an entire micron-wide terrace. In alloys, however, the single metal orientation does not persist across an entire terrace, but a mixture of the two possible lattice orientations, which have a 180° rotational symmetry, are found to coexist within a single terrace. Because regions with distinguishable polarization patterns were not observed in polarization-dependent SHG microscopy, we hypothesize that these domains are smaller than the ~125 nm resolution of the instrument. In our model, if the domains are not spatially resolvable in the far-field, polarization-dependent signals from each domain would be added together to yield the measured nearly isotropic response. This interpretation is supported by the observation that the signal from the spatially distinguish-

https://doi.org/10.1021/acsnano.1c05944
ACS Nano 2021, 15, 17780–17789

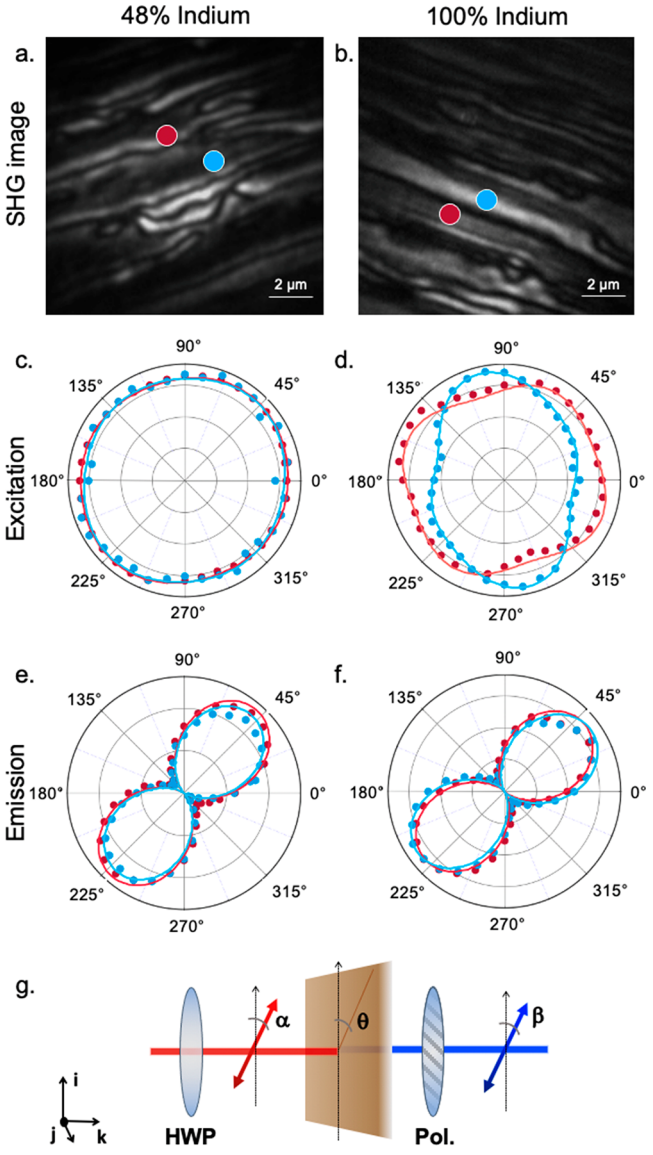

Figure 6. Polarization-dependent SHG-microscopy of 2-D PMets. SHG-detected images of the (a) 2-D alloy and (b) 2-D In show bright regions (terraces) separated by dark areas (step edges). (c and d) Excitation and (e and f) emission polarization-dependent measurements using the experimental setup in panel g from different areas of the sample reveal differences between 2-D alloy and 2-D In.

able domains in 2-D In give a nearly isotropic response when averaged (Figure 7a).

Evidence of increased structural disorder was also obtained from high-resolution scanning transmission electron microscopy (STEM) images of the alloy (Figure 7c,d).[25] Previous statistical analysis of HR-STEM images of 2-D In revealed that the first metal layer is aligned directly above the Si, and the second layer exhibits a strong preference to sit directly above the carbon atoms of the top SiC layer.[14] This preference for a particular registry of the metal atoms over the SiC results in the same metal lattice orientation persisting across an entire terrace. For a 2-D alloy, however, areas in which the first layer of metal is registered with the carbon atoms of the top SiC layer (Figure 7d) are observed, as well as areas with the expected registry over the silicon atoms (Figure 7c). This observation supports our interpretation that the isotropic

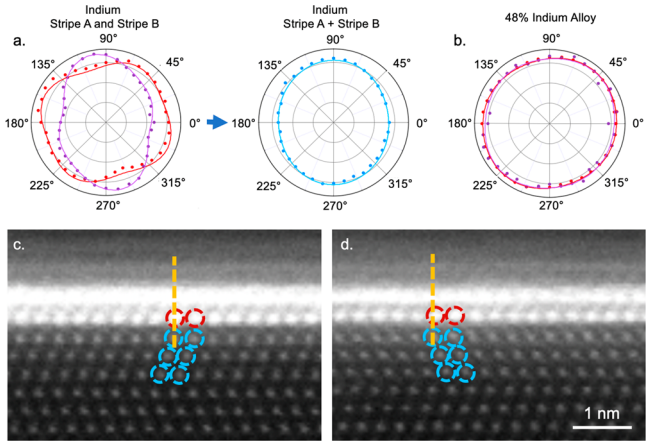

Figure 7. Evidence for structural modifications in 2-D alloys. (a) Averaging over multiple spatial regions in 2-D In yields an isotropic excitation polarization dependence, similar to the polarization dependence of 2-D alloy. High-resolution STEM shows some regions with the first metal layer registered over (c) Si and (d) some regions with the first metal layer registered over C. Circles indicating approximate positions of atoms are a guide to the eye.

excitation polarization dependences result from increased disorder in the Ga/In alloy compared to the single metal system. These results are consistent with the faster electron–phonon scattering time observed in 2-D alloys compared to 2-D In and Ga.

CONCLUSIONS

The dynamics of optically excited electronic carrier relaxation spanning femtosecond to picosecond time scales are reported for 2-D polar metal heterostructures. An initial subpicosecond decay of the transient absorption signal is attributed to electron–phonon scattering. Correlation of transient absorption decay rates and coherent phonon signals with SHG microscopy polar patterns reveals that 2-D alloys display increased disorder compared to the monoelemental systems, which results in 3–5× acceleration of electron–phonon scattering rates for alloys with respect to the monoelementals. We also observe that the rate of interfacial heat dissipation was more efficient for 2-D Ga than for 2-D In. Furthermore, the gallium component determined interfacial energy transfer rates of alloy systems. These results point to prospects for using atomic-level structure to control energy transfer in multicomponent materials through the choice of metal intercalant and alloying conditions. The ability to structurally tune electron–phonon scattering rates to the extent observed for the 2-D heterostructures is difficult to achieve in most conventional 3-D nanoscale and bulk metals. Therefore, the 2-D metals may provide advantages for tailoring applications that require efficient dissipation of thermal energy. Using selective pump–probe wavelength combinations, we also observed picosecond graphene-to-metal carrier transfer. This finding indicates that the metal can efficiently remove energy from graphene, which may be beneficial for mitigating thermal fouling of the capping layer.

EXPERIMENTAL SECTION

Synthesis. 2-D Ga, In, and alloy were obtained *via* the confinement heteroepitaxy (CHet) method in a horizontal tube furnace. The alloy precursor was formed by the mixing of gallium and

https://doi.org/10.1021/acsnano.1c05944
ACS Nano 2021, 15, 17780–17789

indium powder on a custom-made alumina crucible at 80 °C in an Ar environment, and annealing at 800 °C and 500 Torr for 30 min was the optimized condition for the CHet process.[25]

Linear Extinction. Extinction measurements were performed using an Agilent Cary 5000 with a universal measurement accessory. Reflection and transmission spectra were collected with p-polarized light with a 20° incident angle on the sample. Extinction spectra were calculated by extinction = $1 - \%R - \%T$.

Transient Absorption Spectroscopy. The transient absorption instrument used has been described previously.[42] Visible pulses at 100 kHz repetition rate for transient absorption spectroscopy were generated by a noncolinear optical parametric amplifier pumped by a Yb amplifier (Spirit-NOPA, Light Conversion). After collimation and compression with dispersion compensating mirrors, the beam is split into pump and probe arms with a 90/10 beamsplitter. The pump beam travels through a pulse shaper with AOM (2-DQuick-Visible, PhaseTech), which acts as a chopper and along an optical delay line, which sets the pump−probe time delay. The pump and probe are focused onto the sample, and the transmitted probe is collected by a spectrometer (SP2150, Princeton Instruments).

Analysis of transient absorption data was performed using Igor Pro software. Time domain traces were fit to the four-component exponential equation:

$$y(t) = A_1 \cdot \exp(-t/t_1) + A_2 \cdot \exp(-t/t_2) + A_3 \cdot \exp(-t/t_3) + A_4 \cdot \exp(-t/t_4)$$

Four components was the minimum number required to obtain satisfactory fits to the data.

For samples with significant oscillatory features, a damped sine function was incorporated and data were fit to the equation:

$$y(t) = A_1 \cdot \exp(-t/t_1) + A_2 \cdot \exp(-t/t_2) + A_3 \cdot \exp(-t/t_3) + A_4 \cdot \exp(-t/t_4) + A_{\text{osc}} \cdot \exp(-t/t_{\text{osc}}) \sin(2\pi f_{\text{osc}} \cdot t + \varphi)$$

Nonlinear Optical Microscopy. Polarization-resolved SHG microscopy was performed using a previously described method.[14] Excitation pulses at 800 nm with 30 nm bandwidth from a Ti:sapphire laser (Vitara, Coherent) were focused onto the sample with a 0.4 NA aspheric lens. The excitation polarization was adjusted with a half-wave plate placed before the sample. Emission from the sample was collected with a 1.25 NA oil immersion objective (Nikon), and the SHG was isolated from the fundamental and multiphoton photoluminescence using a combination of 400 nm bandpass and 650 nm short-pass filters. An analyzer was used before the detector to determine the polarization of the emitted signal. The signal was imaged and spectrally resolved with an electron-multiplying CCD and coupled spectrometer (iXion Ultra 897/Shamrock 303i, Andor).

SHG microscopy data was analyzed using ImageJ and Igor Pro software. Equations to describe the polarization dependence of the SHG signal have been given previously for our experimental geometry.[14] Excitation polarization-dependent data were fit to the equation:

$$I_{x+y}^{\text{SHG}} \propto [\chi_{xxx}^{(2)} \cos^2(\theta - \alpha) + \chi_{xyy}^{(2)} \sin^2(\theta - \alpha) + 2\chi_{xxy}^{(2)} \sin(\theta - \alpha) \cos(\theta - \alpha)]^2 + [\chi_{yxx}^{(2)} \cos^2(\theta - \alpha) + \chi_{yyy}^{(2)} \sin^2(\theta - \alpha) + 2\chi_{yxy}^{(2)} \sin(\theta - \alpha) \cos(\theta - \alpha)]^2$$

Emission polarization-dependent data were fit to the equation:

$$I(\beta)_{\text{total}}^{\text{SHG}} \propto [\cos(\beta - \beta_0) \cdot P_x^{(2)} + \sin(\beta - \beta_0) \cdot P_y^{(2)}]^2$$

TEM. Cross-sectional transmission electron microscope (TEM) specimens were prepared on a FEI Helios 660 focused ion beam (FIB) system. One kilovolt final cleaning was applied after samples became electron transparent to avoid ion beam damage to the sample surface during FIB. High-angle annular dark field (HAADF) scanning transmission electron microscopy (STEM) was performed on a FEI aberration corrected S/TEM at 300 kV (Titan G2 60-300). Energy-dispersive X-ray spectroscopic (EDS) elemental maps were collected by using a SuperX EDS system (Bruker) under STEM mode.

First-Principles Calculations. The low-frequency phonon modes were assigned using first-principles calculations based on density functional theory (DFT) with the local density approximation[43] to the exchange-correlation functional as implemented in the plane-wave pseudopotential code, QUANTUM ESPRESSO.[44] Optimized norm-conserving pseudopotentials[45] were used, and the alloy was simulated using the virtual crystal approximation (VCA). The atomic structure of the metal bilayers and top five SiC bilayers were obtained by DFT calculations on a slab with two metal layers and six SiC bilayers, passivated by hydrogen atoms at the bottom. Bulk SiC was also simulated. Monkhorst−Pack k-point grids of $26 \times 26 \times 1$ and $26 \times 26 \times 6$ were used, respectively, for calculations involving the slab and bulk SiC. A plane-wave kinetic energy cutoff of 80 Ry and an energy threshold of 10^{-10} Ry was applied for the self-consistent cycle. All atomic positions were relaxed until the forces acting on each atom were less than 0.0001 Ry/Bohr. Coulomb truncation in the z direction for the slab model was applied to ensure the calculations were done in a 2-D framework. Density functional perturbation theory (DFPT) calculations were performed on a $4 \times 4 \times 1$ q-mesh to obtain the force constant matrices of the metal/SiC slabs and bulk SiC. The force constants for the bottom SiC bilayer and H atoms were replaced by the force constant matrix from bulk SiC, and the phonons of the 2-D metal on a semi-infinite SiC substrate were simulated using a recently developed Green's functional approach.

ASSOCIATED CONTENT

Supporting Information

The Supporting Information is available free of charge at https://pubs.acs.org/doi/10.1021/acsnano.1c05944.

Figures of transmission spectra, transient absorption response, data from Figure 2, excitation power-dependent transient absorption data, and phonon DOS at selected wavevectors, computed by the GF method (PDF)

AUTHOR INFORMATION

Corresponding Author

Kenneth L. Knappenberger, Jr. − *Department of Chemistry, Pennsylvania State University, University Park, Pennsylvania 16802, United States;* orcid.org/0000-0003-4123-3663; Email: klk260@psu.edu

Authors

Megan A. Steves − *Department of Chemistry, Pennsylvania State University, University Park, Pennsylvania 16802, United States;* orcid.org/0000-0002-1410-5650

Siavash Rajabpour − *Department of Chemical Engineering, Pennsylvania State University, University Park, Pennsylvania 16802, United States*

Ke Wang − *Materials Characterization Laboratory, Materials Research Institute, Pennsylvania State University, University Park, Pennsylvania 16802, United States*

Chengye Dong − *2D Crystal Consortium, Materials Research Institute, Pennsylvania State University, University Park, Pennsylvania 16802, United States*

Wen He − *Department of Materials Science and Engineering, National University of Singapore, Singapore 117456, Singapore; Centre for Advanced 2D Materials, National University of Singapore, Singapore 117456, Singapore*

Su Ying Quek − *Department of Materials Science and Engineering, National University of Singapore, Singapore 117456, Singapore; Centre for Advanced 2D Materials, National University of Singapore, Singapore 117456, Singapore; Department of Physics and NUS Graduate School Integrative Sciences and Engineering Programme, National*

https://doi.org/10.1021/acsnano.1c05944
ACS Nano 2021, 15, 17780−17789

University of Singapore, Singapore 117456, Singapore; orcid.org/0000-0003-4223-2953

Joshua A. Robinson − *2D Crystal Consortium, Materials Research Institute, Center for 2D and Layered Materials, and Department of Materials Science and Engineering, Pennsylvania State University, University Park, Pennsylvania 16802, United States;* orcid.org/0000-0002-1513-7187

Complete contact information is available at: https://pubs.acs.org/10.1021/acsnano.1c05944

Author Contributions

The manuscript was written through contributions of all authors. All authors have given approval to the final version of the manuscript.

Notes

The authors declare no competing financial interest.

ACKNOWLEDGMENTS

This work was supported by a grant from the Air Force Office of Scientific Research (FA-9550-18-1-0347 and FA9550-19-1-0295) and by the National Science Foundation Graduate Research Fellowship Program under grant no. DGE1255832. This work was also supported by the National Science Foundation under award number CHE-1807999, DMR-2011839, and cooperative agreement DMR-1539916. Funding was also provided by the Singapore National Research Foundation, Prime Minister's Office, under its medium-sized center program. Calculations were performed on the NUS Graphene Research Centre cluster and National Supercomputing Centre Singapore (NSCC).

REFERENCES

(1) Willets, K. A.; Van Duyne, R. P. Localized Surface Plasmon Resonance Spectroscopy and Sensing. *Annu. Rev. Phys. Chem.* **2007**, *58* (1), 267−297.

(2) Halas, N. J.; Lal, S.; Chang, W. S.; Link, S.; Nordlander, P. Plasmons in Strongly Coupled Metallic Nanostructures. *Chem. Rev.* **2011**, *111*, 3913−3961.

(3) Jin, R.; Jureller, J. E.; Kim, H. Y.; Scherer, N. F. Correlating Second Harmonic Optical Responses of Single Ag Nanoparticles with Morphology. *J. Am. Chem. Soc.* **2005**, *127* (36), 12482−12483.

(4) Chandra, M.; Dowgiallo, A. M.; Knappenberger, K. L. Magnetic Dipolar Interactions in Solid Gold Nanosphere Dimers. *J. Am. Chem. Soc.* **2012**, *134* (10), 4477−4480.

(5) Zhang, Y.; Wen, F.; Zhen, Y. R.; Nordlander, P.; Halas, N. J. Coherent Fano Resonances in a Plasmonic Nanocluster Enhance Optical Four-Wave Mixing. *Proc. Natl. Acad. Sci. U. S. A.* **2013**, *110* (23), 9215−9219.

(6) Wang, D.; Guan, J.; Hu, J.; Bourgeois, M. R.; Odom, T. W. Manipulating Light-Matter Interactions in Plasmonic Nanoparticle Lattices. *Acc. Chem. Res.* **2019**, *52* (11), 2997−3007.

(7) Jain, P. K.; Huang, X.; El-Sayed, I. H.; El-Sayed, M. A. Noble Metals on the Nanoscale: Optical and Photothermal Properties and Some Applications in Imaging, Sensing, Biology, and Medicine. *Acc. Chem. Res.* **2008**, *41* (12), 1578−1586.

(8) Liu, L.; Zhou, Z.; Guo, Q.; Yan, Z.; Yao, Y.; Goodman, D. W. The 2-D Growth of Gold on Single-Layer Graphene/Ru(0001): Enhancement of CO Adsorption. *Surf. Sci.* **2011**, *605* (17−18), L47−L50.

(9) Hartland, G. V. Optical Studies of Dynamics in Noble Metal Nanostructures. *Chem. Rev.* **2011**, *111*, 3858−3887.

(10) Arbouet, A.; Voisin, C.; Christofilos, D.; Langot, P.; Fatti, N. D.; Vallee, F.; Lerme, J.; Celep, G.; Cottancin, E.; Gaudry, M.; Pellarin, M.; Broyer, M.; Maillard, M.; Pileni, M. P.; Treguer, M. Electron-Phonon Scattering in Metal Clusters. *Phys. Rev. Lett.* **2003**, *90* (17), 4.

(11) Stagg, S. M.; Knappenberger, K. L.; Dowgiallo, A. M.; Chandra, M. Three-Dimensional Interfacial Structure Determination of Hollow Gold Nanosphere Aggregates. *J. Phys. Chem. Lett.* **2011**, *2* (23), 2946−2950.

(12) Herbert, P. J.; Knappenberger, K. L. Spin-Polarized Photoluminescence in $Au_{25}(SC_8H_9)_{18}$ Monolayer-Protected Clusters. *Small* **2021**, *17* (27), 2004431.

(13) Briggs, N.; Bersch, B.; Wang, Y.; Jiang, J.; Koch, R. J.; Nayir, N.; Wang, K.; Kolmer, M.; Ko, W.; Duran, A. D. L. F.; Subramanian, S.; Dong, C.; Shallenberger, J.; Fu, M.; Zou, Q.; Chuang, Y.-W.; Gai, Z.; Li, A.-P.; Bostwick, A.; Jozwiak, C.; et al. Atomically Thin, Half-van der Waals Metals Enabled by Confinement Heteroepitaxy. *Nat. Mater.* **2020**, *19*, 637.

(14) Steves, M. A.; Wang, Y.; Briggs, N.; Zhao, T.; El-Sherif, H.; Bersch, B. M.; Subramanian, S.; Dong, C.; Bowen, T.; Fuente Duran, A. D. L.; Nisi, K.; Lassauniere, M.; Wurstbauer, U.; Bassim, N. D.; Fonseca, J.; Robinson, J. T.; Crespi, V. H.; Robinson, J.; Knappenberger Jr, K. L. Unexpected Near-Infrared to Visible Nonlinear Optical Properties from 2-D Polar Metals. *Nano Lett.* **2020**, *20* (11), 8312−8318.

(15) Nisi, K.; Subramanian, S.; He, W.; Ulman, K. A.; El-Sherif, H.; Sigger, F.; Lassaunière, M.; Wetherington, M. T.; Briggs, N.; Gray, J.; Holleitner, A. W.; Bassim, N.; Quek, S. Y.; Robinson, J. A.; Wurstbauer, U. Light−Matter Interaction in Quantum Confined 2D Polar Metals. *Adv. Funct. Mater.* **2021**, *31* (4), 2005977.

(16) Mak, K. F.; Lee, C.; Hone, J.; Shan, J.; Heinz, T. F. Atomically Thin MoS_2: A New Direct-Gap Semiconductor. *Phys. Rev. Lett.* **2010**, *105* (13), 136805.

(17) Liu, Y.; Weiss, N. O.; Duan, X.; Cheng, H. C.; Huang, Y.; Duan, X. van der Waals Heterostructures and Devices. *Nature Reviews Materials* **2016**, *1*, 16042.

(18) Rivera, P.; Seyler, K. L.; Yu, H.; Schaibley, J. R.; Yan, J.; Mandrus, D. G.; Yao, W.; Xu, X. Valley-Polarized Exciton Dynamics in a 2D Semiconductor Heterostructure. *Science* **2016**, *351* (6274), 688−691.

(19) Manjavacas, A.; García de Abajo, F. J. Tunable Plasmons in Atomically Thin Gold Nanodisks. *Nat. Commun.* **2014**, *5* (1), 3548.

(20) Sundararaman, R.; Christensen, T.; Ping, Y.; Rivera, N.; Joannopoulos, J. D.; Soljačić, M.; Narang, P. Plasmonics in Argentene. *Phys. Rev. Mater.* **2020**, *4* (7), 74011.

(21) Liao, M.; Zang, Y.; Guan, Z.; Li, H.; Gong, Y.; Zhu, K.; Hu, X. P.; Zhang, D.; Xu, Y.; Wang, Y. Y.; He, K.; Ma, X. C.; Zhang, S. C.; Xue, Q. K. Superconductivity in Few-Layer Stanene. *Nat. Phys.* **2018**, *14* (4), 344−348.

(22) Fujimoto, J. G.; Liu, J. M.; Ippen, E. P.; Bloembergen, N. Femtosecond Laser Interaction with Metallic Tungsten and Nonequilibrium Electron and Lattice Temperatures. *Phys. Rev. Lett.* **1984**, *53* (19), 1837−1840.

(23) Schoenlein, R. W.; Lin, W. Z.; Fujimoto, J. G.; Eesley, G. L. Femtosecond Studies of Nonequilibrium Electronic Processes in Metals. *Phys. Rev. Lett.* **1987**, *58* (16), 1680−1683.

(24) Elsayed-Ali, H. E.; Norris, T. B.; Pessot, M. A.; Mourou, G. A. Time-Resolved Observation of Electron-Phonon Relaxation in Copper. *Phys. Rev. Lett.* **1987**, *58* (12), 1212−1215.

(25) Rajabpour, S.; Vera, A.; He, W.; Katz, B. N.; Koch, R. J.; Lassaunière, M.; Chen, X.; Li, C.; Nisi, K.; El-Sherif, H.; Wetherington, M. T.; Dong, C.; Bostwick, A.; Jozwiak, C.; van Duin, A. C.; Bassim, N.; Zhu, J.; Wang, G.-C.; Wurstbauer, U.; Rotenberg, E.; et al. Tunable Two-Dimensional Group-III Metal Alloys. *Adv. Mater.* **2021**, 2104265.

(26) Nair, R. R.; Blake, P.; Grigorenko, A. N.; Novoselov, K. S.; Booth, T. J.; Stauber, T.; Peres, N. M. R.; Geim, A. K. Fine Structure Constant Defines Visual Transparency of Graphene. *Science* **2008**, *320* (5881), 1308.

(27) Malard, L. M.; Fai Mak, K.; Castro Neto, A. H.; Peres, N. M. R.; Heinz, T. F. Observation of Intra- and Inter-Band Transitions in

the Transient Optical Response of Graphene. *New J. Phys.* **2013**, *15* (1), 015009.
(28) Ahmadi, T. S.; Logunov, S. L.; El-Sayed, M. A. Picosecond Dynamics of Colloidal Gold Nanoparticles. *J. Phys. Chem.* **1996**, *100* (20), 8053−8056.
(29) Hodak, J. H.; Martini, I.; Hartland, G. V. Spectroscopy and Dynamics of Nanometer-Sized Noble Metal Particles. *J. Phys. Chem. B* **1998**, *102* (36), 6958−6967.
(30) Stagira, S.; Nisoli, M.; De Silvestri, S.; Stella, A.; Tognini, P.; Cheyssac, P.; Kofman, R. Ultrafast Optical Relaxation Dynamics in Metallic Nanoparticles: From Bulk-Like toward Spatial Confinement Regime. *Chem. Phys.* **2000**, *251* (1−3), 259−267.
(31) Juvé, V.; Scardamaglia, M.; Maioli, P.; Crut, A.; Merabia, S.; Joly, L.; Del Fatti, N.; Vallée, F. Cooling Dynamics and Thermal Interface Resistance of Glass-Embedded Metal Nanoparticles. *Phys. Rev. B: Condens. Matter Mater. Phys.* **2009**, *80* (19), 195406.
(32) Nisoli, M.; Stagira, S.; De Silvestri, S.; Stella, A.; Tognini, P.; Cheyssac, P.; Kofman, R. Ultrafast Electronic Dynamics in Solid and Liquid Gallium Nanoparticles. *Phys. Rev. Lett.* **1997**, *78* (18), 3575.
(33) Huang, L.; Gao, B.; Hartland, G.; Kelly, M.; Xing, H. Ultrafast Relaxation of Hot Optical Phonons in Monolayer and Multilayer Graphene on Different Substrates. *Surf. Sci.* **2011**, *605*, 1657−1661.
(34) Lin, Z.; Zhigilei, L. V.; Celli, V. Electron-Phonon Coupling and Electron Heat Capacity of Metals under Conditions of Strong Electron-Phonon Nonequilibrium. *Phys. Rev. B: Condens. Matter Mater. Phys.* **2008**, *77* (7), 075133.
(35) Xie, W.; Allioux, F. M.; Ou, J. Z.; Miyako, E.; Tang, S. Y.; Kalantar-Zadeh, K. Gallium-Based Liquid Metal Particles for Therapeutics. *Trends Biotechnol.* **2021**, *39* (6), 624−640.
(36) Dawlaty, J. M.; Shivaraman, S.; Chandrashekhar, M.; Rana, F.; Spencer, M. G. Measurement of Ultrafast Carrier Dynamics in Epitaxial Graphene. *Appl. Phys. Lett.* **2008**, *92*, 042116.
(37) Elsayed-Ali, H. E.; Juhasz, T.; Smith, G. O.; Bron, W. E. Femtosecond Thermoreflectivity and Thermotransmissivity of Polycrystalline and Single-Crystalline Gold Films. *Phys. Rev. B: Condens. Matter Mater. Phys.* **1991**, *43* (5), 4488−4491.
(38) Huang, W.; Qian, W.; El-Sayed, M. A.; Ding, Y.; Wang, Z. L. Effect of the Lattice Crystallinity on the Electron-Phonon Relaxation Rates in Gold Nanoparticles. *J. Phys. Chem. C* **2007**, *111* (29), 10751−10757.
(39) Staechelin, Y. U.; Hoeing, D.; Schulz, F.; Lange, H. Size-Dependent Electron-Phonon Coupling in Monocrystalline Gold Nanoparticles. *ACS Photonics* **2021**, *8* (3), 752−757.
(40) Zeiger, H. J.; Vidal, J.; Cheng, T. K.; Ippen, E. P.; Dresselhaus, G.; Dresselhaus, M. S. Theory for Displacive Excitation of Coherent Phonons. *Phys. Rev. B: Condens. Matter Mater. Phys.* **1992**, *45* (2), 768−778.
(41) Perdew, J. P.; Wang, Y. Accurate and Simple Analytic Representation of the Electron-Gas Correlation Energy. *Phys. Rev. B: Condens. Matter Mater. Phys.* **1992**, *45* (23), 13244−13249.
(42) Giannozzi, P.; Baroni, S.; Bonini, N.; Calandra, M.; Car, R.; Cavazzoni, C.; Ceresoli, D.; Chiarotti, G. L.; Cococcioni, M.; Dabo, I.; Dal Corso, A.; De Gironcoli, S.; Fabris, S.; Fratesi, G.; Gebauer, R.; Gerstmann, U.; Gougoussis, C.; Kokalj, A.; Lazzeri, M.; Martin-Samos, L.; et al. QUANTUM ESPRESSO: A Modular and Open-Source Software Project for Quantum Simulations of Materials. *J. Phys.: Condens. Matter* **2009**, *21* (39), 395502.
(43) Hamann, D. R. Optimized Norm-Conserving Vanderbilt Pseudopotentials. *Phys. Rev. B: Condens. Matter Mater. Phys.* **2013**, *88* (8), 085117.
(44) Bellaiche, L.; Vanderbilt, D. Virtual Crystal Approximation Revisited: Application to Dielectric and Piezoelectric Properties of Perovskites. *Phys. Rev. B: Condens. Matter Mater. Phys.* **2000**, *61* (12), 7877−7882.
(45) Sohier, T.; Calandra, M.; Mauri, F. Density Functional Perturbation Theory for Gated Two-Dimensional Heterostructures: Theoretical Developments and Application to Flexural Phonons in Graphene. *Phys. Rev. B: Condens. Matter Mater. Phys.* **2017**, *96* (7), 075448.

https://doi.org/10.1021/acsnano.1c05944
ACS Nano 2021, 15, 17780−17789